Materials Science & Engineering A 857 (2022) 144050

Contents lists available at ScienceDirect

Materials Science & Engineering A

journal homepage: www.elsevier.com/locate/msea

The effects of surface finish on the fatigue performance of electron beam melted Ti–6Al–4V

L. Ednie [a], R.J. Lancaster [a,*], A.A. Antonysamy [b], F. Zelenka [c], A. Scarpellini [c], L. Parimi [b], R. Maddalena [c], N.C. Barnard [a], P. Efthymiadis [b]

[a] Institute of Structural Materials, Bay Campus, Swansea University, Swansea, SA1 8EN, UK
[b] GKN Global Technology Centre, Additive Manufacturing Group, Taurus Road – Patchway, Bristol, BS34 6FB, UK
[c] Thermo Fisher Scientific, Achtseweg Noord 5, 5651 GG Eindhoven, the Netherlands

ARTICLE INFO

Keywords:
Electron beam melting
Ti–6Al–4V
Fatigue
Surface roughness

ABSTRACT

Additive manufacturing (AM) is an advanced manufacturing technique whose uptake within the aerospace industry is being limited by the lack of understanding of the effects of surface finish on the fatigue properties of AM built components. It is known that the surface profile of as-built AM parts is significantly rougher than its traditionally manufactured equivalent, promoting stress raising features that have an adverse effect on fatigue life.

This paper will focus on developing a deeper understanding of the fatigue properties of the widely-used alpha-beta titanium alloy, Ti–6Al–4V, as manufactured through electron beam melting (EBM) and the role that surface roughness plays. Results have been generated on as-built and machined & polished EBM test coupons, supported by microstructural and fractographic analysis, X-ray computed tomography (XCT), advanced surface profilometry and hardness testing.

Results have shown that as-built EBM Ti–6Al–4V samples have a significantly inferior fatigue life than machined & polished samples, despite the material in each of the surface finish types being hot isostatically pressed (HIP). It has been revealed that while surface parameters, MR_2 and R_a, provide no correlation to high cycle fatigue life, it is shown that as the R_p surface parameter decreases, the respective number of cycles to failure increases. It can be concluded that a samples' surface roughness is a highly contributing factor in influencing fatigue performance, yet it should not be considered in isolation since other features, including porosity, also play an important role.

1. Introduction

Additive manufacturing (AM) is a relatively modern method of component manufacture that has seen significant growth in its use over recent years [1]. AM is a process that fabricates near net shape components by fusing multiple layers of metallic powders together using a high energy heat source. Electron beam melting (EBM) is one such method, where a high energy electron beam acts as the heat source to selectively melt material in order to successively build a 3D component [2]. This process of fusing together metallic powders, layer by layer is thought to have many advantages across many different sectors, particularly the aerospace industry, as it can lead to significant fuel savings by reducing component weight and waste material, and also allows for the redesign of components to reduce the number of parts being fused together to manufacture the finished article [3]. EBM also offers the added benefit of producing components with insignificant residual stresses due to the raised temperature of the build plate during the production process.

Even though AM has many benefits, these limitations on the mechanical properties such as fatigue life due to the high surface roughness of components is still limiting this technique's further adoption. This is one of the main limitations that is seen within AM components as the increased surface roughness in as-built components is much greater than that of the wrought or cast equivalent. The surface roughness seen in EBM components is also considerably higher than that of samples produced using other AM methods due to the use of faster scan speeds, larger powder sizes and thicker build layers [4].

Within the EBM build process, metallic powder is initially raked

* Corresponding author.
E-mail address: r.j.lancaster@swansea.ac.uk (R.J. Lancaster).

https://doi.org/10.1016/j.msea.2022.144050
Received 18 July 2022; Received in revised form 25 August 2022; Accepted 19 September 2022
Available online 25 September 2022

across the build plate and then pre-heated to an elevated temperature before the powder is melted. The melting of the layer using the electron beam can be broken down into two stages of contouring and hatching. It is the contouring of the part that controls the quality of the surface and therefore the surface roughness. Within the EBM process, there are two methods of contouring: non-multispot contouring and multispot contouring. Contouring sees the melting of the component outline and is undertaken to provide a barrier between the component and the surrounding powder [5].

Non-multispot contouring is a continuous melting process, where the electron beam moves continuously along the outer edge of the component to melt the layer of the build. It has been previously observed that the speed of the electron beam and the beam current can have a significant effect on the surface roughness of the component with non-multispot contouring. Multispot contouring sees the high energy electron beam moving rapidly to keep multiple melt pools active at any one time. This is achieved by splitting up the outer edge of the component into a smaller and shorter section before the beam will then 'spot' an outer edge and subsequently move to the next 'spot'. Spotting is the melting of a section of material as small as the diameter of the electron beam and only for a very short amount of time [5].

Generally, non-multispot contouring provides a better surface finish than multispot contouring but the more optimised surface finish comes at the expense of the component's dimensional accuracy; while multispot contouring gives better dimensional accuracy, it also results in a higher surface roughness [5]. This high surface roughness leads to the formation of surface-breaking stress raising features, which have an adverse effect on the fatigue properties of a material and can be attributed to the staircase effect, partially melted powder particles or the balling phenomenon [6].

The surface roughness of a sample can be referred to as the variations in height along the sample surface in relation to the samples' reference plane [7]. It is also important to highlight the difference between surface roughness and surface waviness. While surface roughness is referred to as small variations along the surface related to the surface reference, waviness is the more widely spaced measure of surface texture, upon which surface roughness is found [8].

In previous literature, the differences in surface roughness have been discussed, with Nicoletto et al. splitting surface roughness into primary and secondary roughness effects [9]. It is thought that primary roughness is a result of powder particle size and the inherent build parameters of the AM process, such as layer thickness and melt track geometries, whereas secondary roughness is the result of partially melted powder particles on the component surface. In this work, it was concluded that the negative effect that surface roughness has on the fatigue properties of EBM components is as a result of primary roughness alone, as secondary roughness only attributes to ~10 μm of the R_a value of the component, whereas primary roughness can be attributed to up to the maximum powder particle size used [9,10].

Through the exploration of successful methods to effectively quantify the surface roughness of as-built EBM material and correlate the roughness to the component's fatigue life, it has been found that certain surface parameters can effectively rank the fatigue life of a component. This has been explored in previous literature, where correlations between surface parameters and component fatigue life have been discussed [11–13]. From this it was found that height roughness parameters give the strongest correlation to high cycle fatigue (HCF) life, and that surface data values such as R_a and R_t are not efficient, relatively, when it comes to quantifying fatigue performance in the nickel based superalloy, Inconel 718 [14]. In a more holistic and cross-cutting study, Sanaei et al. found that correlations between parameters such as R_p, MR^2, and R_v provided a stronger correlation to a materials' HCF life than parameters such as R_a and R_t across an array of materials [15]. It is known that the areas of high surface roughness such as valleys on the surface act as area of stress concentration zones and these features then act to replicate micro-notches on the as-built surface of AM components. The depth of these valleys on the surface can be analysed and the shape profiled to link these valleys to a stress concentration factor (K_t), to provide an accurate representation of the knockdown seen on a component's fatigue life due to the surface roughness. This has been successfully demonstrated in work carried out by Pegues et al. [16].

Typically, components produced using AM for high-end applications require an average surface roughness of less than 1 μm. This therefore indicates that a high surface roughness is one of the main limiting factors of using AM components within critical applications in the aerospace industry. Even though these features cannot be removed completely through the optimisation of the method's process parameters, they can be reduced or removed by carrying out post-processing methods such as machining and polishing [17]. It has also been noted in previous studies that even though surface roughness is the main contributor to a reduction in fatigue life within AM components, it cannot be considered alone [3]. Alongside the surface roughness, the presence of internal features such as entrapped gas porosities or areas of lack of fusion (LoF) must also be considered as these can also have a negative effect [18].

In this paper, the effects of altering the surface finish of hot isostatically pressed (HIP) EBM Ti–6Al–4V samples will be investigated to consider the influence of an as-built surface finish in comparison to material finished with a polished surface, under HCF. The results of the fatigue experiments will also be supported by advanced surface profilometry, microstructural and fractographic studies, X-ray computed tomography and further mechanical testing and sample porosity analysis.

2. Materials and experimental methods

2.1. Material

In this research, a series of EBM Ti–6Al–4V (full alloy composition given in Table 1) hourglass fatigue samples were built vertically in the 90° orientation on a theme 5.0 ARCAM Q20+ machine using the default build process parameters as suggested by ARCAM. These samples were produced with a build layer thickness of 90 μm, a particle size between 42 and 102 μm and an apparent powder density of 2.54 g/cm^3, taken from three separate powder batch measurements. The powder distribution of the Ti–6Al–4V powder used to produce the samples detailed within this report can be seen in Fig. 1. Post-build, these samples were subjected to a hot isostatic pressing (HIP) treatment (920 °C ± 10 °C, 102 MPa for 120 min) to reduce the presence of any internal features such as porosity which could have an adverse effect on fatigue life.

A selection of 20 EBM Ti–6Al–4V samples were built in line with the axial fatigue – cylindrical sample drawing taken from BS EN6072:2010, as displayed in Fig. 2 [19]. Due to some of these samples requiring post-process machining & polishing, ten samples were built with stock additions of 1.52 mm, so when machining and polishing was completed the sample geometries remained consistent. Along with this, prior to testing, cross sectional area measurements were taken for each individual sample to ensure conformity and the application of consistent stress values to samples with differing surface finishes.

To modify the surface finish in these samples, a selection of ten samples were subjected to a longitudinal machining & polishing procedure in line with BS EN6072:2010 to remove any evidence of the rough surface finish, while the other ten samples remained in the as-built condition [19]. The difference in the two surface conditions used within this research can be seen in Fig. 3, with Fig. 3a showing the as-built surface condition while Fig. 3b presents the machined & polished condition. For the purpose of this research, as-built samples have

Table 1
Nominal composition of Ti–6Al–4V alloy (wt.%).

Al	V	Fe	C	N	O	Ti
6.57	3.96	0.20	0.01	0.01	0.2	Bal

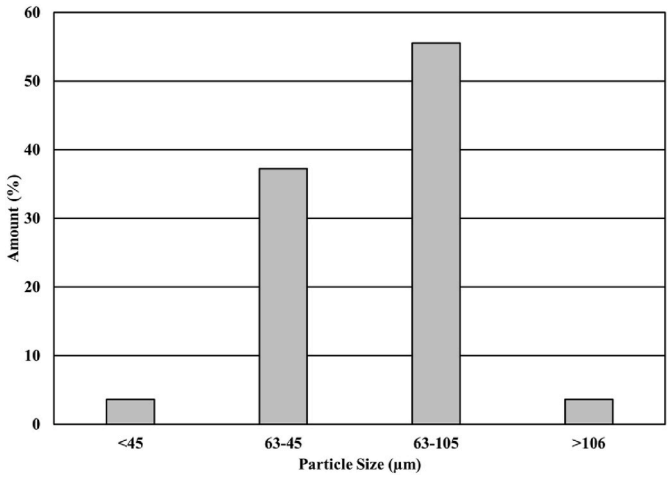

Fig. 1. Powder distribution size of EBM Ti–6Al–4V powder.

been numbered from 1 to 10 and machined & polished samples 11 to 20.

2.2. Surface roughness

Surface roughness measurements were recorded on an Alicona G5 Focus Variation microscope to gather data on the surface parameters of the samples. The Alicona system uses focus variation with the combined depth of focus of an optical microscope, aided by a vertical scanning movement to provide topographical data on the variation of focus. The vertical resolution can be as low as 10 nm using the Alicona. Post scan analysis is subsequently carried out using the Infinite Focus Measurement Suite by Alicona. Four surface roughness measurements were taken at various positions around the circumference of the samples covering an area of approximately 13 × 2 mm.

Various surface roughness parameters including the R_a (average surface roughness profile), R_p (maximum peak height of roughness profile) and MR_2 (the fraction of a surface that will carry a load) were recorded for each specimen analysed. All measurements were carried out in compliance with ISO 21290 for roughness [20].

2.3. Fatigue testing

Constant amplitude HCF tests were carried out using an R-ratio of 0.1 and a frequency of 5 Hz under a sinusoidal load control waveform. All tests were carried out at room temperature using an Instron servo-hydraulic test frame, under a range of maximum applied stress values to generate a suitable stress (σ_{max}) – number of fatigue cycles to failure (N_f) curve. The diameter of each sample's gauge length was measured at multiple points using a shadowgraph and the applied σ_{max} values were calculated in accordance with ISO Standard 1099:2017 for axial force-controlled fatigue testing of metallic materials [21].

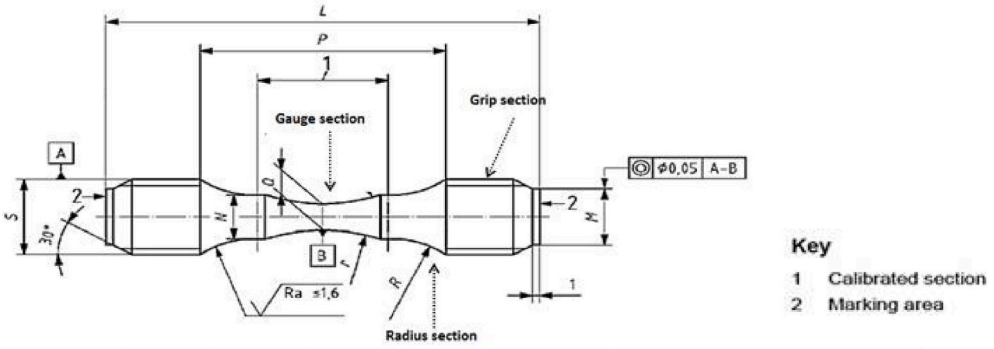

L (mm)	M (mm)	N (mm)	P (mm)	Q* (mm)	R (mm)	S	r* (mm)
80	13	10	48	5.64±0.03*	20	M16 Pitch 100	40±1.0*
General Tolerance			Js 12				
Form Tolerance			IT 9				

Fig. 2. EBM Ti–6Al–4V cylindrical fatigue specimen drawing in line with BS EN6071:2010 [19].

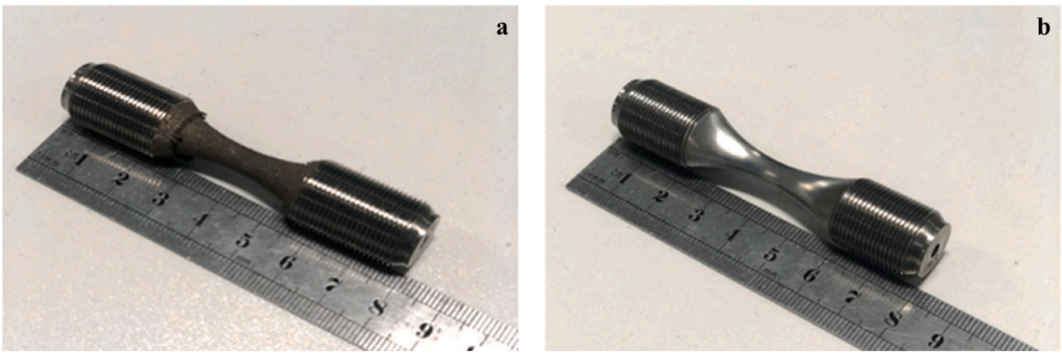

Fig. 3. EBM Ti–6Al–4V HCF samples **a.** as-built, and **b.** machined & polished surface finishes.

2.4. Vicker's hardness testing

Vicker's hardness testing of five as-built and five machined & polished samples was carried out prior to fatigue testing using a Struers Duramin-40 Automated Hardness Tester. These tests were carried out under a force of 1 kg to limit the potential variation within hardness values and a dwell time of 10 s. In accordance with BS EN 6507:2005, there was a 1 mm spacing between each indentation, with 100 indentations being made on each tested sample in a 10 × 10 grid, with each 10 values being averaged [22].

2.5. Microstructure and fractographic analysis

The microstructure and fracture surfaces of the vertically built EBM Ti–6Al–4V HCF specimens were characterised using a Zeiss Evo scanning electron microscope (SEM). Microstructural analysis was carried out on a sample orientated in the X–Y plane (perpendicular to the vertical build direction) and a sample orientated in the X-Z plane (parallel to the build direction), allowing for the differences in microstructure due to the thermal process of EBM samples to be examined. Prior to SEM analysis, samples were sectioned, ground and polished to a mirror-like finish before being etched using Kroll's reagent to reveal the microstructure. To ensure that clear images of the fracture surfaces could be taken, all fracture surfaces prior to SEM analysis were cleaned beforehand with acetone in an ultrasonic bath for 20 min at a temperature of 45 °C to remove any loose debris or dirt from the surface. If any features i.e., striations, were found upon a sample's fracture surface, these could be analysed and measured using Image J. The samples taken from the alternative orientations were also examined via EBSD analysis. This allowed for the determination of texture within the EBM samples to be observed but could also be used to measure and quantify grain size.

Digital optical microscopy was also carried out to determine if the presence of internal defects such as porosity had an influence on fatigue performance. This was undertaken on a Zeiss Smartzoom 5, and porosity calculations were carried out using ImageJ software. This was performed on a selection of as-built (6 and 8) and machined & polished samples (17 and 18) to capture the most extreme results in both cases. With these four samples, four different sections from each were analysed. For this investigation, each sample of sectioned material was mounted in a conductive mounting compound prior to being ground and polished to reveal a flat mirror like surface from which the presence of porosity could be detected.

2.6. Micro X-ray computed tomography (XCT)

Micro XCT analysis was performed on a sample with each of the surface finish conditions to gain a cross-sectional view of the specimens and to reveal any internal areas of interest such as unfused powder particles and porosity.

The XCT scans were taken on HeliScan Micro XCT system using 160 kV of energy and a current of 27 μA. For each scan, an exposure time of 11 s per shot was used and 3392 projections were recorded. A series of filters were employed to optimise the resolution, including a 6 mm aluminium and a 1 mm stainless-steel thick plate. Each scan took ~13 h, with a minimum voxel resolution of 4.1 μm being achieved. The reconstruction time was 5 h.

3. Results and discussion

3.1. Microstructure

It is well known that Ti–6Al–4V is the most widely used alpha (α) and beta (ß) titanium alloy within the aerospace industry, offering a favourable strength to weight ratio [23]. It is also one of the most highly used metallic powders within AM processes. Due to the complex thermal cycle experienced during the AM build process and the resultant epitaxial grain growth, the microstructure seen in the X–Y plane and the X-Z plane of a sample usually differs. The images presented in Fig. 4 show the X–Y orientation (Fig. 4a) and X-Z orientation (Fig. 4b) of the vertically built Ti–6Al–4V EBM samples used within this research.

Due to the thermal cycles experienced in the EBM process, as expected, the X–Y orientated sample, which runs perpendicular to the vertical build direction shows an ordered and equiaxed beta microstructure while the X-Z orientated sample running parallel to the vertical build direction, appears to show evidence of a columnar beta grain structure. It can be seen in Fig. 4a of the sample orientated in the X–Y plane that a fine needle-shaped lath morphology can be seen, which is then also seen within the columnar grain structure of the sample orientated within the X-Z plane in Fig. 4b.

The microstructure in both images show that these samples consist mainly of the α phase, with a small amount of retained ß phase. The ß phase can be seen retained within prior columnar ß grains, which surround needle like α laths [4]. Due to the columnar nature of the α laths, random measurements were taken of the α widths and lengths from three images of each orientation and averaged in line with ASTM E112-13 [24]. These measurements, alongside a mean liner intercept measurement, have been included in Table 2, containing microstructural measurements to allow for the analysis and comparison of the microstructures seen in Fig. 4.

From Table 2, it can be seen that when calculated using the mean linear intercept method and multiple individual measurements of the α lath widths and heights, that the average α lath size in both the X–Y orientation and the X-Z orientation are very similar. Using EBSD, inverse pole figure (IPF) maps of the X–Y and the X-Z planes can be compared, as seen in Fig. 5. These maps allow for the determination of the crystallographic orientation of each sample, while grain boundary maps can be readily seen in band contrast maps displayed in Fig. 6. Grain boundaries can have an influence on a materials' mechanical properties so these maps can be used to display grain boundaries based upon angles of misorientation. The IPF maps of the two alternative orientations show a basketweave microstructure with the columnar morphology now more evident in the X-Z orientation (Fig. 5b). The secondary dendrites are also apparent in this orientation, which typically result from the high cooling rate experienced during the rapid solidification process of EBM. In both orientations, most of the α laths have a random orientation.

From the grain boundary maps of the X–Y and X-Z orientations seen in Fig. 6, grain boundary angles and α lath sizes can be determined. It is known that there is a relationship between the α lath size, the yield strength and fatigue life. Lucas et al. found that as the α lath size decreases, the material yield strength increases which then gives rise to an improved fatigue performance [25]. In this research, the α laths had a greater average area in the X-Z orientation than was seen in the X–Y orientation.

3.2. Surface roughness

Previous literature has found that certain surface roughness parameters exhibit a stronger influence on the HCF behaviour of AM components [14]. It has been reported that height surface parameters give the strongest correlation to HCF life, whilst surface parameters such as R_a and R_t do not provide an accurate representation or correlation to the fatigue life of AM materials [14]. It is expected that this is due to the multiple layers that are fused together to build an AM component and the lack of accurate repeatability with R_a values. Therefore, within this work, attention has been paid to the R_p and the MR_2 surface parameters, where the R_p value gives a representation of the maximum peak or valley height within a roughness profile, while the MR_2 value represents the fraction of a surface that will carry a load. The profile scans recorded using Alicona surface profilometry on as-built and machined & polished samples can be seen in Fig. 7a and Fig. 7b respectively. The surface roughness parameters recorded from this are displayed in Table 3. Even though a sample's R_a value isn't deemed as an accurate representation of

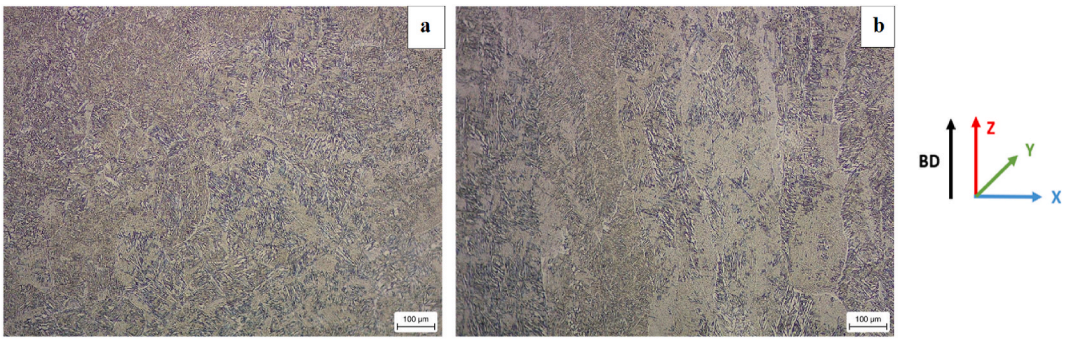

Fig. 4. Microstructure of EBM Ti–6Al–4V samples in the **a.** X–Y orientation, and **b.** X-Z orientation.

Table 2
Microstructural measurements of EBM Ti–6Al–4V.

Measurement	X–Y Orientation	X-Z Orientation
Average Mean Linear Intercept (1/μm)	4.00	4.01
Average α Lath Width (μm)	2.09	2.14
Average α Lath Length (μm)	12.23	13.74

a sample's surface roughness, this parameter has also been included given that this measure is still regarded as one of the most recognised terms when evaluating surface roughness. It should also be noted that other surface parameters were also considered within this study, but strong correlations were not noted.

From Table 3, it can be seen that for the as-built samples, sample 8 has the highest R_p value at 121.29 μm, while sample 6 has the lowest R_p value of 91.93 μm. The overall average R_p value for specimens with an as-built finish is 109.53 μm. Within the group of machined & polished

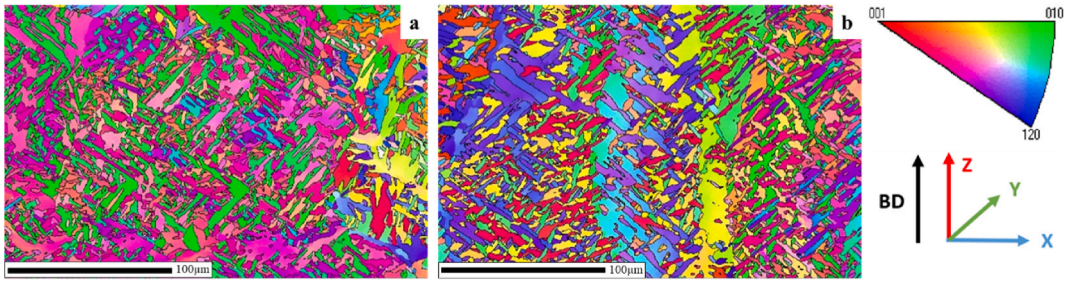

Fig. 5. EBSD IPF maps of **a.** X–Y orientation, and **b.** X-Z orientation.

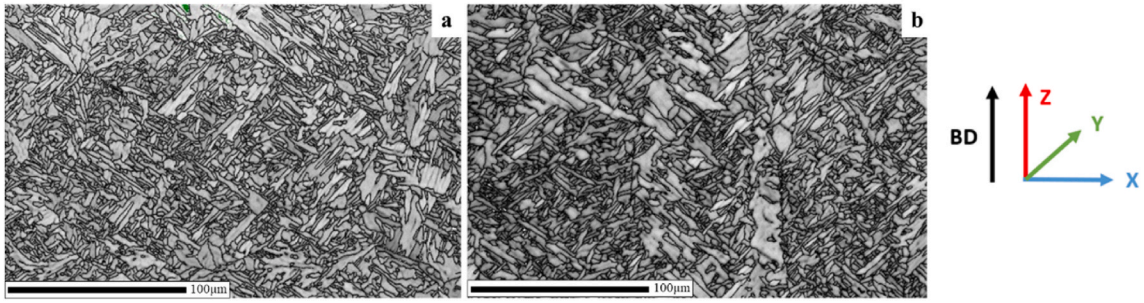

Fig. 6. EBSD grain boundary contrast maps of **a.** X–Y orientation, and **b.** X-Z orientation.

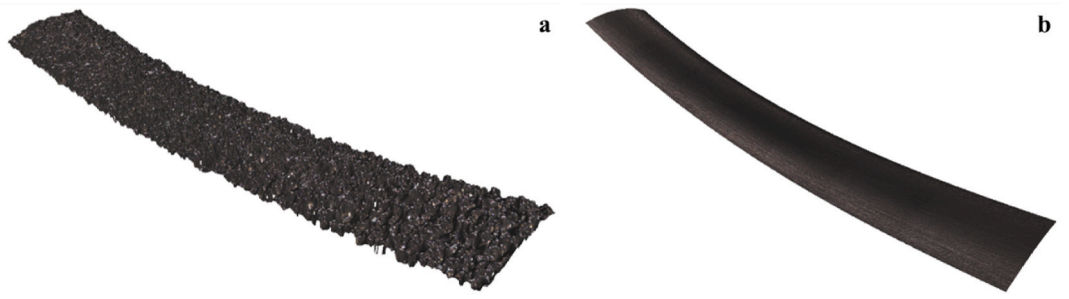

Fig. 7. Alicona surface roughness profiles for EBM Ti–6Al–4V HCF samples with **a.** as-built surface, and **b.** machined & polished surface.

Table 3
Surface roughness parameter data for as-built and machined & polished samples.

As-Built Samples				Machined & Polished Samples			
Sample Number	R_p (μm)	MR_2 (%)	R_a (μm)	Sample Number	R_p (μm)	MR_2 (%)	R_a (μm)
1	118.83	88.13	37.82	11	2.03	90.27	0.90
2	110.96	89.11	36.54	12	2.46	90.12	1.63
3	117.01	89.79	38.88	13	1.85	92.56	1.47
4	114.87	88.46	34.67	14	3.43	88.92	3.11
5	107.90	87.42	37.49	15	2.12	89.13	1.13
6	91.93	89.21	33.89	16	2.73	92.96	3.07
7	106.57	89.37	34.77	17	2.83	87.45	1.70
8	121.29	88.28	40.10	18	1.60	86.80	2.94
9	112.63	88.61	30.95	19	1.65	86.02	2.92
10	93.84	88.98	27.70	20	2.93	84.29	0.84
Average	109.53	88.74	35.28	**Average**	2.36	88.85	1.97

Table 4
HCF performance as a function of maximum applied stress in as-built and machined & polished EBM Ti–6Al–4V samples; R = 0.1, 5Hz.

As-Built Samples			Machined & Polished Samples		
Sample Number	σ_{max} (MPa)	N_f	Sample Number	σ_{max} (MPa)	N_f
1	600	6284	11	600	6,092,199
2	250	125,930	12		
3	450	21,240	13	750	1,698,388
4	175	537,037	14	800	622,229
5	300	82,480	15	800	719,778
6	300	118,328	16	800	637,202
7	200	769,780	17	600	5,893,268
8	300	35,247	18	600	11,881,986
9	300	71,805	19	700	3,698,612
10	300	90,420	20	700	3,842,303

samples, the highest and lowest R_p values are held by samples 14 and 18 with R_p values of 3.43 μm and 1.60 μm respectively, with significantly less variance found across the range of samples analysed and a far lower overall average of 2.36 μm. Due to the nature of the machining & polishing procedure, it is expected that this would remove the vast majority of the variation within the height profiles and as such, result in a lower overall R_p value. Through the removal of variation within the height profile of a sample, it is expected that this will result in the sample being able to withstand a greater number of cycles to failure and higher σ_{max} values, due to the removal of stress-raising features which act to promote fatigue initiation and failure. Therefore, it can be predicted that the machined & polished samples will have a fatigue life greater than that of the as-built samples. Due to the difference in surface finish, the MR_2 values for as-built and machined & polished samples cannot be directly compared to each other, but samples within each group can be ranked if all samples were tested under the same testing conditions. Within the group of as-built samples, it would be expected that sample 5 would offer the worst fatigue performance as it has the lowest MR_2 value of 87.42%, whilst sample 3 would exhibit the best fatigue performance with an MR_2 value of 89.79%, with these samples having an overall average MR_2 value of 88.74%. The prediction of best and worst performing specimens can also be made for the machined & polished samples, with sample 16 predicted to give the best fatigue performance with an MR_2 value of 92.96%, whilst in contrast, with the lowest MR_2 value of these samples of 84.29%, sample 20 would be expected to fail after the shortest number of fatigue cycles if these samples were tested under the same testing conditions. Overall, the machined & polished samples have an average MR_2 value of 88.85%.

When considering the R_a values for both sample groups, it can be seen that again the average R_a value for as-built samples is significantly higher at 35.28 μm than the equivalent value for the machined & polished samples at 1.97 μm. If a sample's fatigue performance was determined by their respective R_a value, within the as-built samples sample 10 would be predicted to perform best with an R_a value of 27.7 μm and sample 8 would have the worst performance with an R_a value of 40.10 μm. Similarly, for the machined & polished samples this would result in sample 20 being envisaged on having the best fatigue performance while sample 14 would perform worse, with R_a values of 0.84 μm and 3.11 μm respectively.

3.3. High cycle fatigue

The fatigue behaviour of all tested EBM Ti–6Al–4V samples in both the as-built and machined & polished surface conditions is presented in Table 4. This data can also be seen in a graphical form of $\sigma_{max} - N_f$ in Fig. 8. Alongside the plotted data points, the surface parameters for each tested sample have also been noted. From the data seen in Table 4 and Fig. 8, a general expected trend can be seen. This trend shows that as the σ_{max} value increases, N_f decreases, irrespective of the surface finish of the sample. When comparing the fatigue behaviour of the as-built samples to those in the machined & polished condition, it can be seen that the machined & polished samples can withstand greater σ_{max} values. In literature, it is thought that a machined & polished sample tested at the same σ_{max} as an as-built sample, would be able to withstand 3x the number of cycles [26]. Considering a direct comparison of an as-built sample (sample number 1) and a machined & polished sample (sample number 11) tested under identical conditions ($\sigma_{max} = 600$ MPa), it can be seen that the machined & polished sample can withstand nearly 1000x the cycles to failure of the as-built sample, which is a significantly greater performance than expected.

From Fig. 8, it can be seen that the range of σ_{max} values over which the as-built samples were tested is larger compared to the machined & polished equivalents. Within this range, sample 1 was tested at a σ_{max} of 600 MPa but failed after 6284 cycles, but it is seen that by reducing the applied σ_{max} value to 175 MPa, as was performed on sample 4, that even in the as-built condition, 537,037 cycles were completed prior to failure. In the HCF tests on the machined & polished samples, the σ_{max} range within which these samples have been tested is much smaller, owing to the more consistent nature of the surface finish, with machined & polished samples tested between 600 MPa and 800 MPa, achieving a fatigue life ranging from 6,092,199 to 62,229 cycles respectively.

As denoted in Fig. 8, the surface roughness parameters are detailed for each sample. This allows for a relationship between the surface parameters, σ_{max} and N_f to be considered. A series of as-built samples were tested under the same conditions ($\sigma_{max} = 300$ MPa) and it can be seen that as the R_p value decreases, the number of fatigue cycles necessary to generate failure increases. Sample 8 has an R_p value of 121.29 μm and withstood 35,247 cycles prior to failing, sample 9 then saw a decrease in R_p value to 112.63 μm and an increase in N_f to 71,805 cycles. This was again seen in samples 5 and 10, which had decreasing R_p values of 107.90 μm–93.84 μm respectively which allowed the number of cycles to failure to increase from 82,480 to 90,420 cycles, respectively. It can also be seen that sample 6, having a higher N_f than sample 10, also has a lower R_p of 91.93 μm. This analysis shows that as the maximum height across the samples decreases, an improvement in the sample's fatigue life is observed.

In a parallel study for the machined & polished condition, three samples, namely 14, 15 and 16, were all tested under the same applied stress ($\sigma_{max} = 800$ MPa). Sample 14 was able to withstand 62,229 cycles before failure with an R_p value of 3.43 μm, whereas sample 16 had an R_p value of 2.73 μm but an increase in the number of cycles to failure of 637,202 cycles. This correlation in decreasing R_p value to the number of cycles to failure was once again seen with sample 15, which had a decreased R_p value of 2.12 μm and an increased number of cycles to failure of 719,778. Similarly, three further samples (11, 17 and 18) were tested under the same conditions at 600 MPa. Like that seen for the samples tested at 800 MPa, as the measured R_p value decreases, an increase in the resulting N_f was observed. Within both sample sets, the MR_2 and the R_a value showed no discernible correlation with N_f and

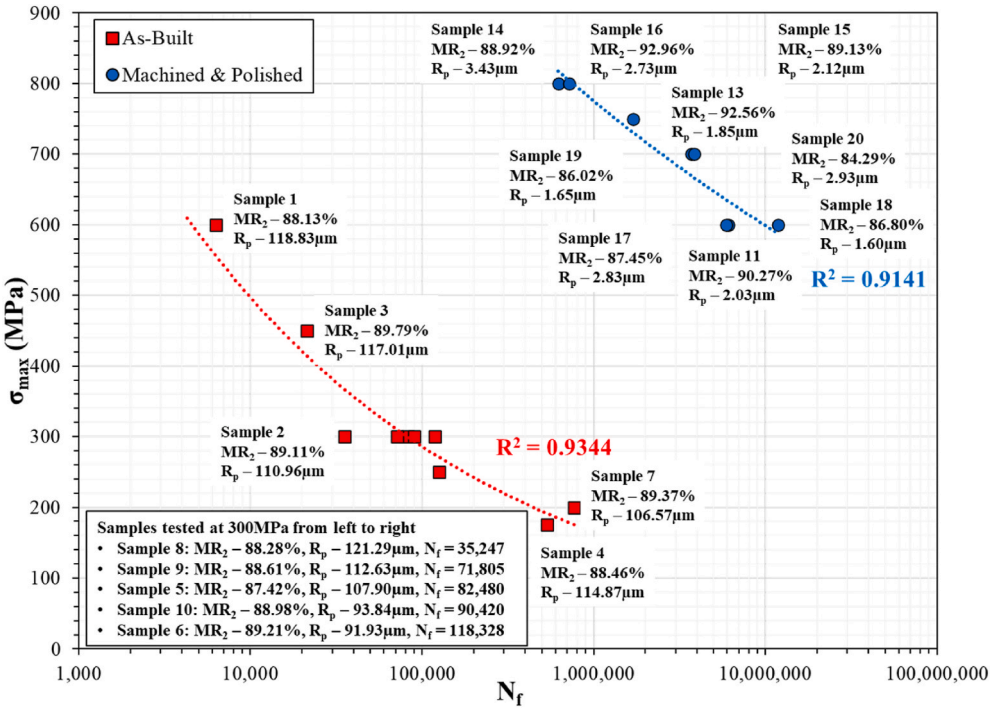

Fig. 8. Fatigue life vs. maximum applied stress of HIP EBM Ti–6Al–4V as-built and machined & polished EBM Ti–6Al–4V HCF samples; R = 0.1, 5Hz.

σ_{max}. It is also important to acknowledge that given the high values of R^2 that have been derived for each respective σ_{max}-N_f curve ($R^2 = 0.9344$ for as-built and $R^2 = 0.9141$ for machined & polished), experimental scatter must also be considered to be a contributing factor to any variation in the fatigue lives observed and variation between individual data points can not be attributed to surface roughness alone.

In Fig. 9 the fatigue data gathered for the EBM Ti–6Al–4V samples in both the as-built and machined & polished conditions tested in this research, is compared to fatigue data collected from a published source on conventional cast and wrought Ti–6Al–4V material [27]. From this, it can be seen that the as-built samples are performing significantly worse than conventional material, which can be attributed to the samples' poor surface finish. It can also be seen that in most cases the machined & polished EBM Ti–6Al–4V samples are performing better than conventional cast and wrought material, except for sheet material at stresses below 700 MPa. The data for sheet, bar and castings have been taken from a single source, however it is important to note that other published sources have found higher levels of fatigue life scatter in wrought Ti–6Al–4V [28,29]. Chern et al. actually found a greater level of scatter in the fatigue lives in the conventional and machined Ti–6Al–4V as opposed to the EBM equivalent, but the conventional material did primarily offer a superior fatigue resistance [28]. Rao et al. undertook a

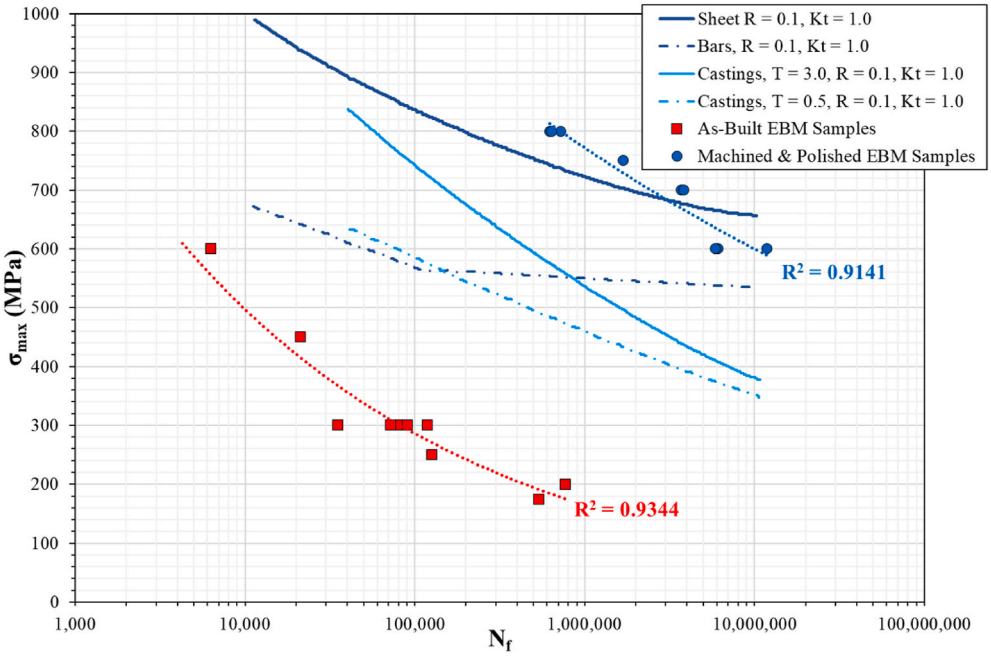

Fig. 9. Fatigue behaviour of as-built and machined & polished EBM Ti–6Al–4V samples compared to conventional cast and wrought data reproduced from Ref. [27].

more extensive review of such scatter and found that for conventional Ti–6Al–4V, a significant variation in fatigue is observed, with a spread of fatigue lifetime of more than two orders of magnitude for most levels of applied stress [29]. Indeed, for a given number of cycles to failure, the scatter in fatigue strength is more than 400 MPa for most of the data set.

3.3.1. Scanning electron microscopy

Fracture surface images of all the as-built fatigue tested samples are shown in Fig. 10. It can be seen from these images that in the majority of the as-built samples, more than one surface breaking initiation site is present. In these samples, a dominant initiation zone can be identified by the larger nature of these sites compared to other surface-breaking features, exhibiting a semi-circular, thumbnail-like appearance that is present on the outer edge. A high magnification image of a typical surface breaking initiation feature, as found in sample 1, is given in Fig. 11. The primary initiation zone on these samples shows great variation in size ranging from 706.86 μm^2 to 1890 μm^2 in area with the height variation across the fracture surfaces of these samples ranging from 1.04 mm to 2.23 mm.

It can be seen from Fig. 10a, that there are multiple surface initiation sites present on sample 1, exhibiting the highest number of initiation sites of the tested as-built samples however, it did not have the highest R_p or MR^2 value. It can be inferred from these samples that there is no correlation between the number of initiation sites and the surface roughness of these samples. It would be expected that were there to be a correlation between the number of surface breaking fatigue initiation sites on a sample and the R_p or MR_2 value, that sample 8 would have the higher number of initiation sites as it has the highest R_p value, and sample 6 would have the least. However, this relationship ceases to exist in this study.

Fig. 12 presents the fracture surface images for the HCF machined & polished samples, where the samples have failed mainly due to sub-surface features that have acted to initiate a fatigue crack. In most cases, these can be seen to initiate from large star-like features, where crack growth appears to propagate radially, and a high magnification image of one of these features, seen in sample 19, is displayed in Fig. 13. The initiating zones seen in the tested machined & polished samples have a surface area ranging from 1010 μm^2 to 2220 μm^2. When comparing the contrasting fracture surfaces, a further observation can be seen when analysing the level of plasticity seen in the two specimen types. The fracture surfaces of the as-built specimens are predominantly flat, exhibiting signs of reduced ductility, whereas the machined &

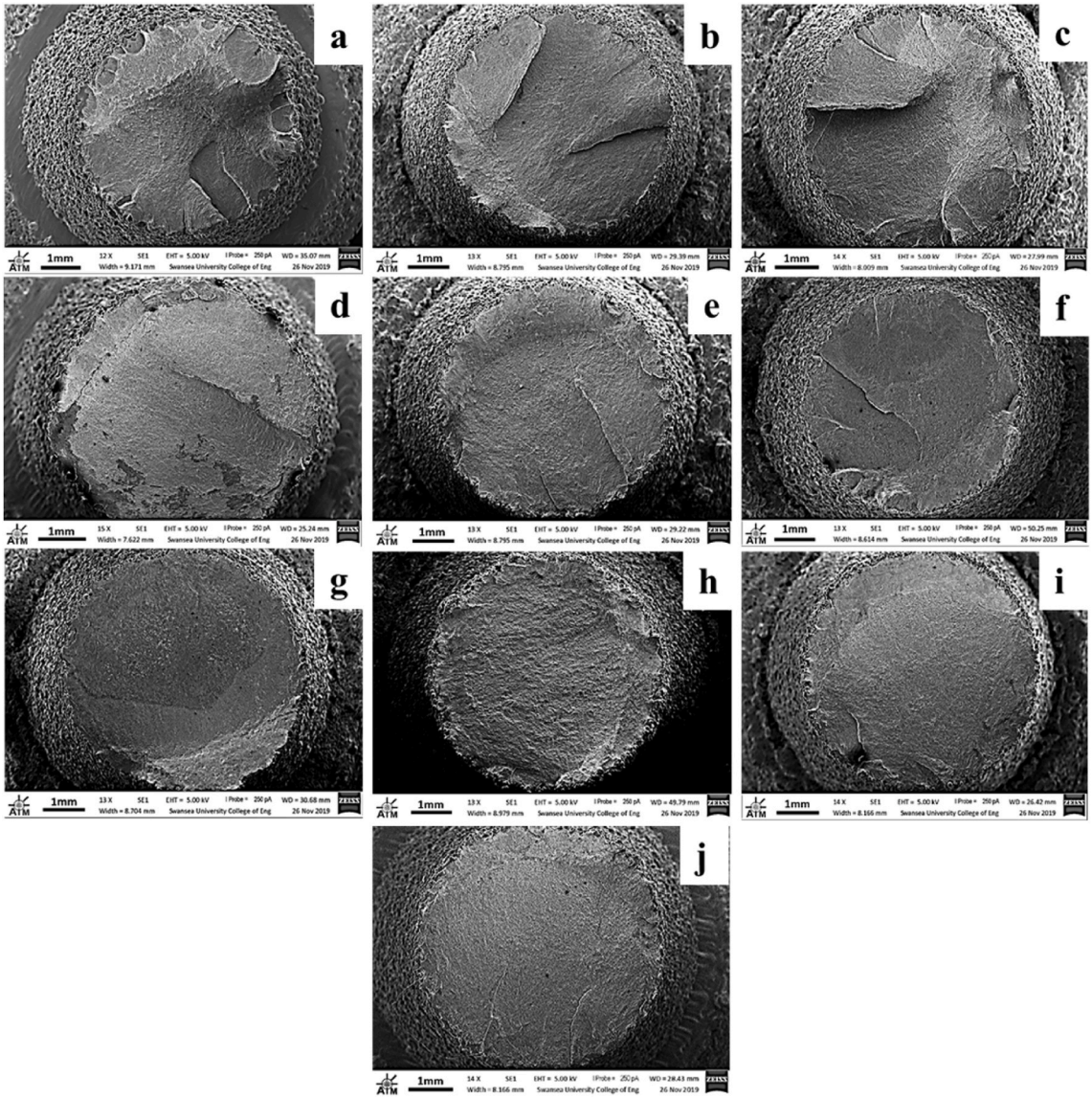

Fig. 10. SEM images of as-built fracture surface of **a. – j.** corresponding to samples 1–10 respectively. sample 1, **b.** sample 2, **c.** sample 3, **d.** sample 4, **e.** sample 5, **f.** sample 6, **g.** sample 7, **h.** sample 8, **i.** sample 9, **j.** sample 10.

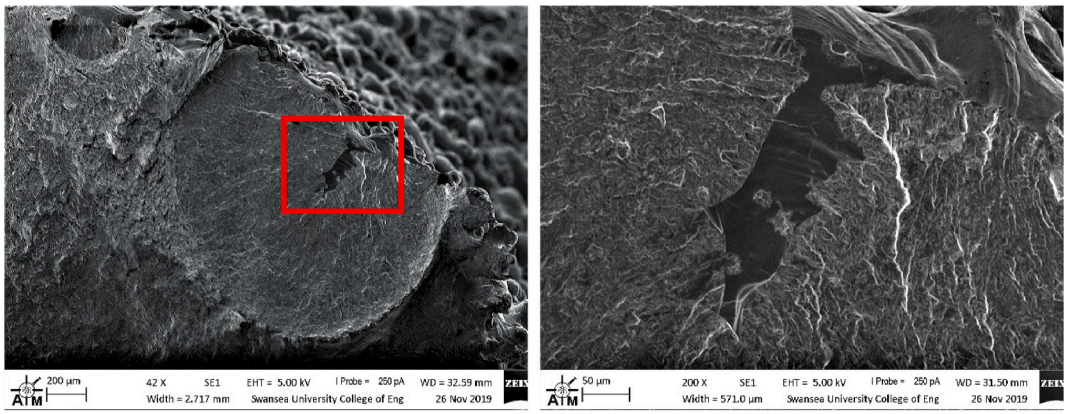

Fig. 11. High magnification image of a surface breaking initiation feature seen in sample 1.

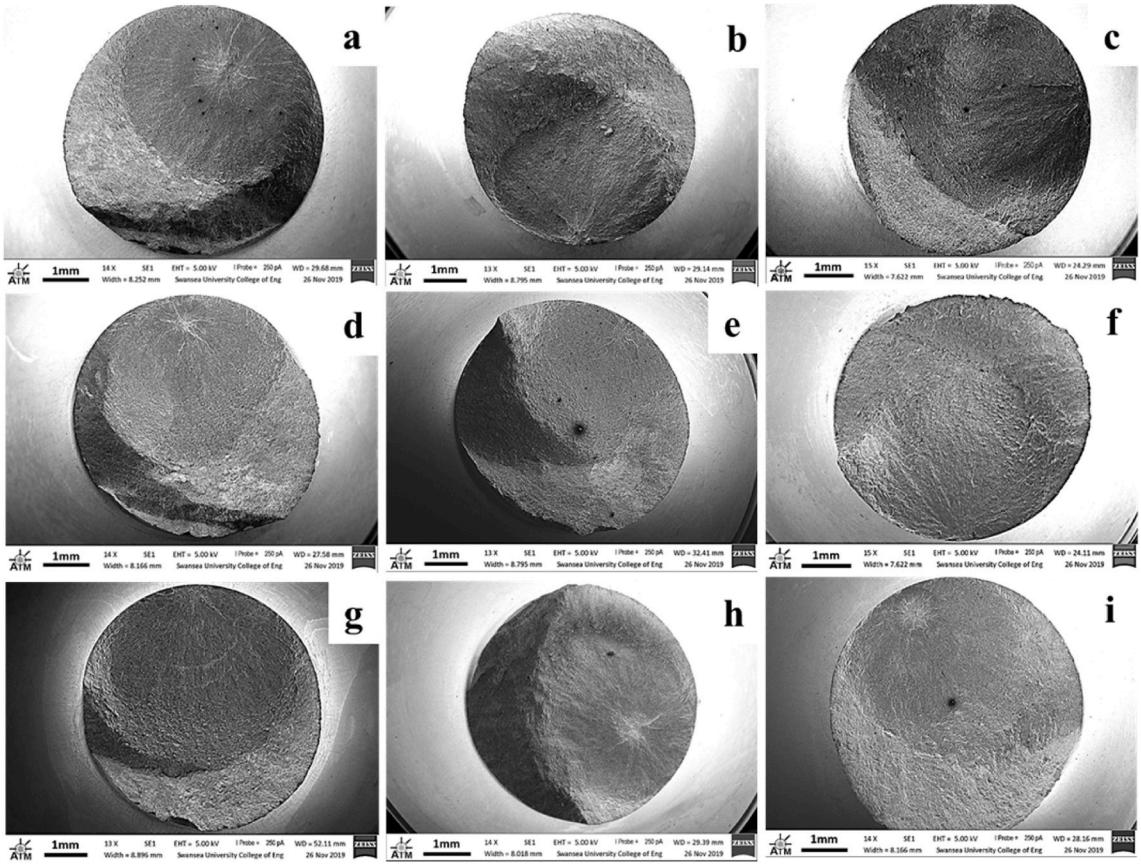

Fig. 12. SEM images of machined & polished fracture surface of **a.** sample 11 b sample 13 **c.** sample 14 **d** sample 15 **e.** sample 16 **f.** sample 17 g sample 18 **h** sample 19 **i.** sample 20.

polished specimens fail in a more ductile manner as evidenced by the increased levels of shear lips seen around the periphery of the surface, with the variation in fracture surface height ranging from 2.59 mm to 3.64 mm. The phenomenon of shear lips occurring is likely because the machined & polished specimens have a single dominant crack that propagates through the component until the ligament that is still intact experiences an overload failure. The crack growth phase gives way to tearing which results in that elevated shear lip that is often at approximately 45°. This phenomenon is slightly different from the as-built surface specimens since there are multiple cracks initiating around the circumference of the component and so the overload is experienced internally to the specimen and not on the specimen edge.

The presence of characteristic fatigue features can be seen on the fracture surfaces of both the as-built and machined & polished EBM Ti–6Al–4V samples. These features include striations and surface cracking, which gives insight into the rate of fatigue crack growth [30]. Typical striations found upon the fracture surface of both as-built and machined & polished samples can be seen in Figs. 14 and 15, respectively. The striations have been captured in two different regions to determine if the rate of crack propagation changes as the distance from the crack initiation zone increases. Both Figs. 14a and 15a show the striations on the fracture surface at a region close to the fatigue crack initiation site while Figs. 14b and 15b have been imaged in a region slightly further from the initiation site, to allow for the difference and

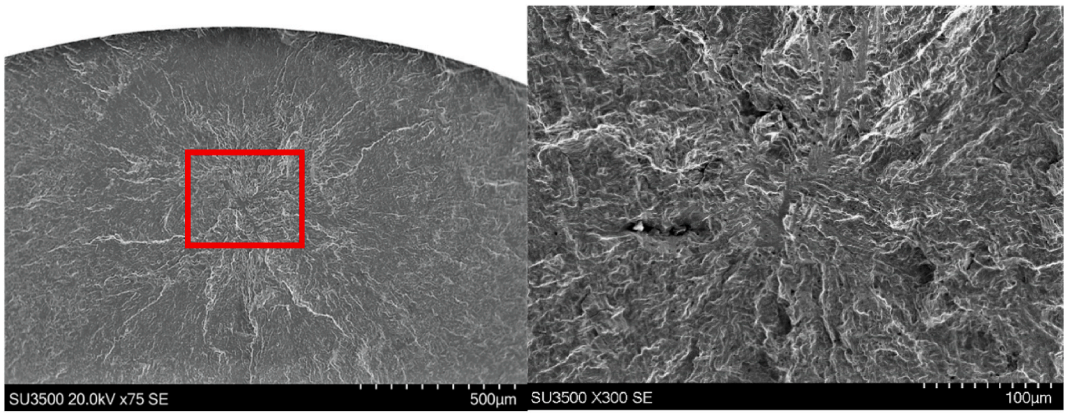

Fig. 13. High magnification image of a sub-surface initiation zone seen in sample 19.

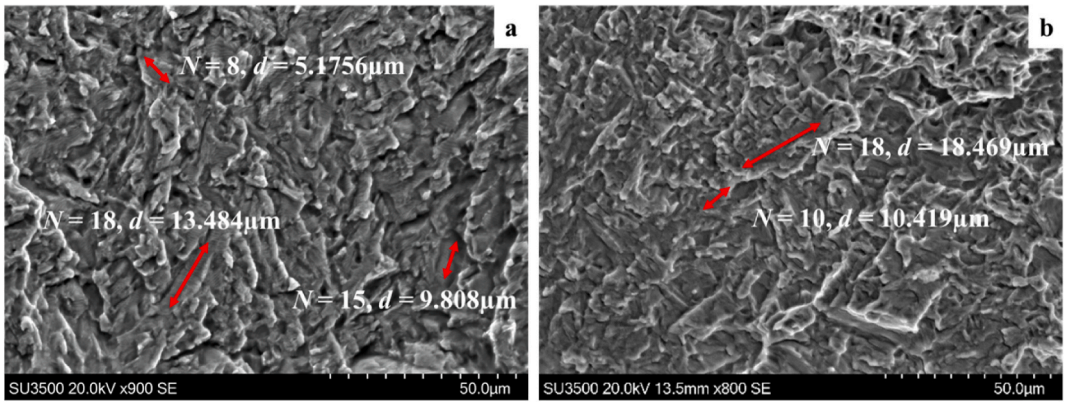

Fig. 14. Presence of striations on the fracture surface of as-built sample 1, **a.** close to initiation site **b.** further from initiation site. *N* refers to the number of striations, *d* is the distance between each striation recorded.

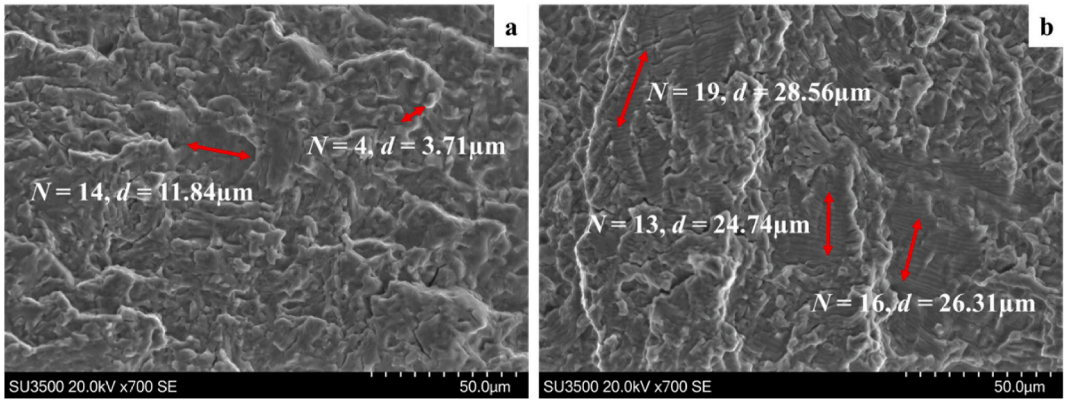

Fig. 15. Presence of striations on the fracture surface of machined & polished sample 20, **a.** close to initiation site **b.** further from initiation site. N refers to the number of striations, d is the distance between each striation recorded.

acceleration in the rate of crack propagation to be determined.

Analysis of the striation spacings displayed in Fig. 14a show that for the as-built specimen, in the location adjacent to the crack initiation site (~680 µm from centre of initiation zone), the spacing between each striation is smaller than that seen further along the crack, as presented in Fig. 14b (~820 µm from the centre of the initiation zone). The striation spacing in Fig. 14a is at an average of 0.683 µm while the striation spacing in Fig. 14b averages at 0.913 µm, indicating an increased rate of crack growth as the crack accelerates to failure.

This is seen again with the images of striations seen in the machined & polished sample, as given in Fig. 15. Here, it can be clearly seen that the striation spacing increases as the crack moves away from the initiation zone of the specimen. The images in Fig. 15a and b have been taken at regions 1.04 mm and 1.43 mm away from the primary initiation site. It is calculated that earlier in the crack the striation spacing averages at 0.887 µm (as shown in Fig. 15a), while in Fig. 15b the average striation spacing doubles, increasing to 1.684 µm. With this increase in spacing between each progressive striation, this shows an increase in the rate of crack growth as the crack moves further from the initiation zone.

3.4. Micro XCT

Micro XCT images were captured of the longitudinal cross section of each surface variation to determine whether there was any presence of porosity, internal features, or surface breaking cracks that could influence the fatigue performance of the EBM Ti–6Al–4V samples. The cross-sectional image of as-built sample 1 can be seen in Fig. 16a while the cross section of machined & polished sample 18 can be seen in Fig. 16b and c.

From the image presented in Fig. 16a, it can be seen that the as-built sample shows the presence of multiple surface breaking cracks that have propagated towards the centre of the sample. These cracks have typically initiated from regions of high stress, which are likely to be multiple given the coarse nature and high roughness of the as-built surface finish. It can be assumed that the crack on the lower right side of sample 1 initiated prior to the other two cracks highlighted given that it exhibits a crack length of 1.32 mm as compared to the others which measure at 0.731 mm and 0.274 mm respectively.

From the XCT cross-sectional image of the machined & polished sample, as given in Fig. 16b and c, it can be determined that there are very few, if any, sites for cracks to propagate from the surface and very few internal features that lead to the concentration of stress that could potentially promote a premature initiation of a fatigue crack. Although the sample in Fig. 16b does not show the presence of any surface breaking cracks, the presence of a pore with a diameter of 0.125 mm can be seen in the inset image given in Fig. 16c.

3.5. Numerical simulation

In an attempt to understand the influence that the surface finish of the as-built condition has upon the stress state during HCF testing, simple two-dimensional simulations were performed using finite element analysis (FEA). A general static, axisymmetric model was created using Abaqus, where the surface finish captured via optical imaging was overlayed onto the nominal specimen dimensions. The conversion of the surface finish to a series of sketch entities was carried-out for a series of 4 sectioned samples. 8-node biquadratic axisymmetric elements, CAX8, were used in the simulations and boundary conditions were applied to achieve the nominal test peak stress, σ_{ref} = 300 MPa. More than 45,000 elements were used to characterise the surface detail, and in excess of 60,000 elements were used in the presence of internal defects. Typical material properties for wrought Ti–6Al–4V were used in the elastic analyses. A tentative value for stress concentration factor, K_t, was determined according to $K_t = \sigma_{yy}/\sigma_{ref,y}$. The refence stress as a function of specimen height can be seen in Fig. 17a for the specimen dimensions given in Fig. 2. An example of the tentative stress concentration in areas of interest are given in Fig. 17b, ignoring free surface and singularities present: yielding predicted K_t values between 1 and 3. Elevated stress levels and K_t values are observed at near-surface regions close to the greatest depressions at the surface (K_t~3) and extend into the specimen bulk, suggesting that the material yield stress would be exceeded at many sites along the gauge. The geometrically sharpest pits present at the surface area are predicted to give rise to a K_t of greater than 12, which is only reduced to 10 when alternatively approximated by a small radius. It is acknowledged that this 2D, axisymmetric model represents a worst-case scenario in terms of the as-built surface (Fig. 7), however it supports the observed debit in HCF fatigue performance of as-built specimens compared to machined and polished test pieces of equivalent geometry (Fig. 8).

Fig. 18 shows the predicted von Mises stress field throughout a separate section taken from an as-built test specimen. It is readily apparent that the surface from this section was less coarse in terms of pits and protrusions from the simulation presented in Fig. 17, however, there was a significant increase in the amount of build defects present in the macroscale image, including porosity throughout the section in addition to features of lack of fusion close to the surface. When considering the influence of the locations of these features it is apparent that those residing closest to the surface have a more pronounced effect on the stress field, compared to equivalent sized pores in the specimen bulk. Indeed, the greatest areas of significantly elevated stress regions are present in Fig. 18, corresponding to areas where build defects – primarily porosity – are in close proximity to a surface pit/depression, presenting opportunity for crack formation. In terms of high cycle fatigue performance, it is suggested in Fig. 18 that the likelihood of fatigue initiation from the largest defect present, particularly subsurface, would be reduced.

3.6. Porosity

Porosity calculation data from the as-built and machined & polished fatigue samples with the most extreme fatigue lives at a given stress level are presented in Table 5. In these results, it can be seen that porosity has an apparent effect on fatigue life. When comparing the average porosity count and percentage area of porosity in as-built samples 6 and 8, it can be seen that sample 6 has an average porosity count of 19 pores (percentage area of 0.003–0.010%) and completed 118,328 cycles prior to failure, while sample 8 has an average of 396 pores (percentage area of 0.0163–0.186%) and completed 35,247 cycles upon failing. These results indicate a significant correlation between porosity and fatigue life, as the two samples were tested under the same loading conditions (σ_{max} = 300 MPa), but sample 6 exhibited a fatigue life more than three times greater than sample 8.

A lesser trend can be determined from the porosity count and total percentage area of porosity of the machined & polished samples 17 and

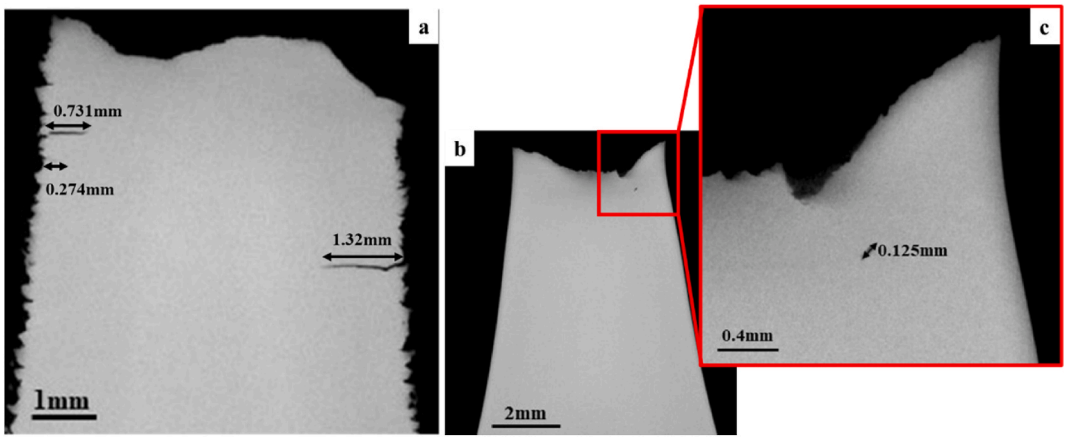

Fig. 16. Micro XCT longitudinal cross-sectional images of EBM Ti–6Al–4V **a.** as-built sample 1, and **b.** machined & polished sample 18, **c.** inset image of Fig. 16b.

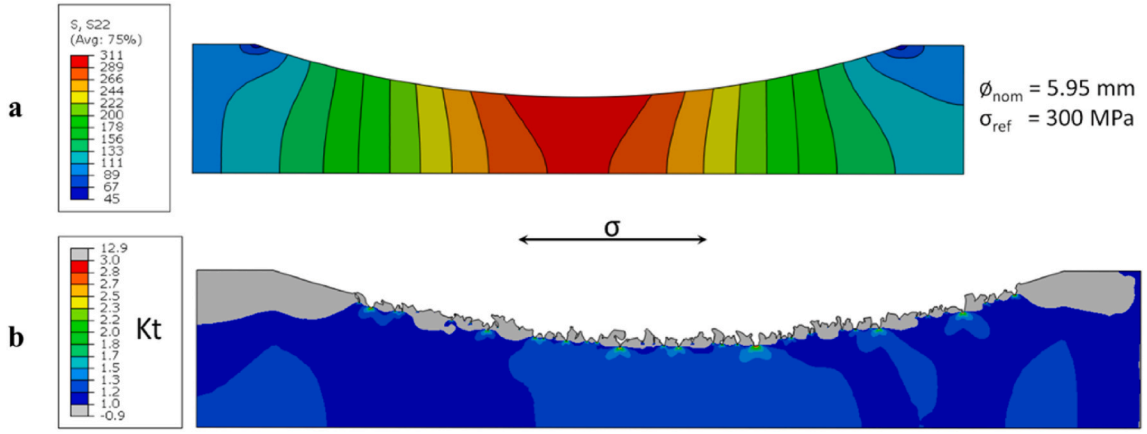

Fig. 17. FEA simulation of an as-built surface finish **a.** σ_{ref} as a function of specimen height and **b.** stress concentrations on specimen surface.

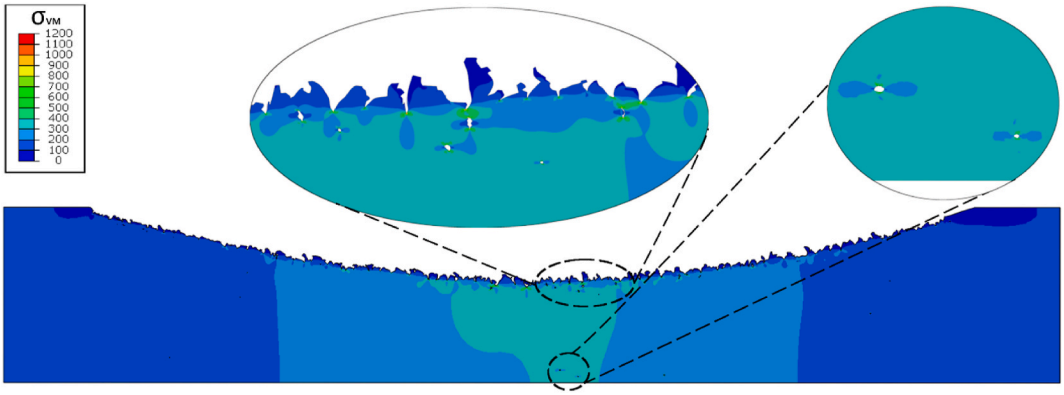

Fig. 18. von Mises stress under imposed conditions of σ_{ref} = 300 MPa. Inset – areas denoting the stress field around near-surface and subsurface build artefacts; porosity, lack of fusion, etc.

Table 5
Porosity data for as-built (samples 6 & 8) and machined & polished (samples 17 & 18) EBM Ti–6Al–4V samples. A-D refer to perpendicular sections through the respective specimens at relative quartile locations, where A represents the lowest location and D the highest.

Sample ID	σ_{max} (MPa)	N_f	Porosity Count	Average Porosity Count	% Area	Average Feret Diameter (μm)	Largest Pore Area (μm^2)
6A	300	118,328	20	19	0.010	5.82	38.95
6B			8		0.003	4.23	42.85
6C			42		0.008	3.26	23.37
6D			7		0.003	5.08	31.16
8A	300	35,247	460	396	0.150	3.85	58.43
8B			419		0.113	3.71	42.31
8C			655		0.186	3.66	50.64
8D			48		0.016	4.31	19.48
17A	600	5,893,268	34	45	0.010	3.35	23.37
17B			31		0.010	3.79	29.31
17C			89		0.023	3.10	77.91
17D			25		0.009	4.10	42.85
18A	600	11,881,986	7	31	0.002	4.31	11.69
18B			40		0.022	4.09	23.73
18C			5		0.001	2.79	3.90
18D			72		0.053	4.69	54.54

18, which were both HCF tested at a σ_{max} of 600 MPa. Sample 17 completed 5,893,268 cycles with an average porosity count of 45 pores (percentage area of 0.009–0.023%), while sample 18 failed after 11,881,986 cycles with an average of 31 pores (percentage area of 0.001–0.053%).

Across the two variations of surface finish, it can be seen that generally the porosity count determined for the machined & polished samples is lower than that of the as-built samples and therefore, it can be deduced that the effect of porosity on the as-built samples' fatigue life would be expected to be greater. Furthermore, there is a direct correlation between an increase in porosity size and a decrease in fatigue life.

3.7. Surface to bulk hardness

Vicker's hardness tests were performed on selected as-built and machined & polished samples in order to analyse how the mechanical properties change from the surface to the interior bulk material. These results are presented in Table 6 and Fig. 20 for the as-built samples, and

Table 7 and Fig. 21 for the machined & polished samples. In total 100 indentations were made on each sample in a 10 × 10 formation with a 1 mm spacing between each indent. Once all indentations were complete, an average hardness value was calculated for each row of 10 indentations, where each row ran from the surface (location 1) to the bulk material (location 10). The indentation pattern taken from surface to bulk material can be seen in Fig. 19.

As given in the results displayed in Table 6 and Fig. 20, it can be seen that there is minimal variation in the hardness values from each samples' surface to the material bulk and with the exception of as-built sample 9, all samples sit within a range of 20 Hv from the highest hardness value to the lowest. Sample 7 can be seen to have the smallest variance from its highest hardness value (324 Hv – 1 mm from the surface) to its lowest hardness value (305 Hv – 3 mm from the surface) of 19 Hv. Only a very slightly higher difference is seen in sample 9, which has the largest difference in hardness values of 22 Hv.

The surface to bulk hardness results for the selected machined & polished samples are given in tabulated form in Table 7 and graphically in Fig. 21.

As material has been removed from the surface of machined & polished samples and the material has been plastically deformed, it is possible that work hardening has been introduced that affects the surface of these samples, which could act to increase a sample's fatigue life. However, it can be seen that there is minimal variation in the Vicker's hardness of machined & polished samples, like that observed in the as-built samples. From Table 7 and Fig. 21, it can be seen that the hardness values for the machined & polished exhibit a smaller range of Hv values than in the as-built samples. The lowest variation within the hardness values of these machined & polished samples was seen in sample 15 with a difference of only 13 Hv from its highest hardness values at 299 Hv (2 mm from the surface) to its lowest hardness value at 285 Hv (1 mm from the surface). It is also seen that sample 11 has the largest range of Hv values across a sample with a difference of 22 Hv, which ranges from the highest hardness value at 302 Hv (3 mm from the surface) to the lowest value of 279 Hv (2 mm from the surface). Overall, even though the machined & polished samples have hardness values within a smaller range than the as-built samples, the variation of hardness in all samples sits within a range of less than 10%.

When comparing the hardness data presented for the two surface finishes, a ± 10% variation in hardness values for the as-built samples is observed, whilst there is only a ± 3% variation in the machined & polished samples. It can also be noted within the as-built samples that the hardness values are generally elevated at the surface, which then decrease as they approach the bulk material before increasing again in the bulk material. This relationship is similar to the findings reported by Lesko et al., who found that a relationship exists at the surface of the material between the hardness values and the process parameters of the build. Their study was undertaken on laser powder bed fused IN718 and revealed that microhardness was highest at the surface of the build and deep within the bulk material, yet between these two regions, a drop in hardness was observed [31]. This behaviour was attributed to the relationship between the scan strategy of the build and the thermal effects seen in additively-manufactured components. This relationship is not seen as clearly within the machined & polished samples due to the removal of 1.52 mm stock addition. Whilst this change in hardness value alludes to a relationship between geometric location and hardness value, it is not expected to have a significant effect on a sample's fatigue life.

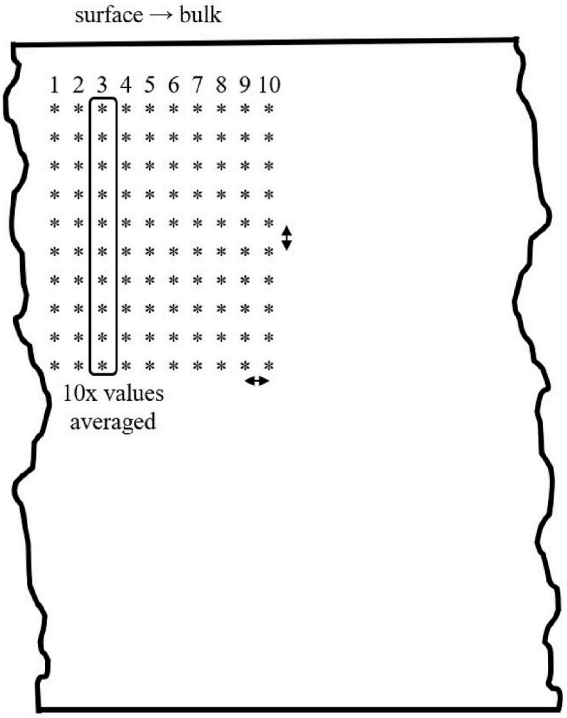

Fig. 19. Location of surface to bulk material hardness testing (not to scale).

3.8. Summary

The data and results presented demonstrates that a samples' surface roughness has a considerable influence on fatigue life. However, it is apparent that surface finish should not be considered in isolation due to other features likely to be present in the component. This was determined using laboratory-scale specimens tested under HCF at repeated stress conditions, which were subsequently analysed to identify whether there were any subsurface, process-induced features contributing to the respective fatigue performance of the test-piece, or whether there was a significant variation in hardness that could indicate a localised change in microstructure and therefore mechanical properties, which could also influence fatigue behaviour. It was found that the volume of porosity adversely affected the final fatigue life of both as-built, and machined & polished samples, contributing to a reduction in life of two and three orders of magnitude in the samples analysed. In regards to the hardness profiles, it can be seen that there was a difference in range between the two surface finishes and can be noted that there is a relationship seen between hardness value and geometric location on a rough as-built surface, in line with the findings reported by other researchers [10,15,31–33].

Table 6
Average Vicker's hardness results for EBM Ti–6Al–4V as-built samples. The first result for each specimen represents the indentation taken as close as possible to the surface location, but within the area requirements suitable for hardness testing.

Sample	Hardness Hv										Stnd Dev
	1	2	3	4	5	6	7	8	9	10	
1	311	301	296	294	304	310	314	313.92	311	305	6.75
3	287	279	276	278	287	291	282	272	281	284	5.41
5	311	298	292	296	293	297	301	307	302	311	6.61
7	324	323	313	308	308	308	311	305	311	317	6.15
9	282	281	283	270	261	275	268	281	274	277	6.79

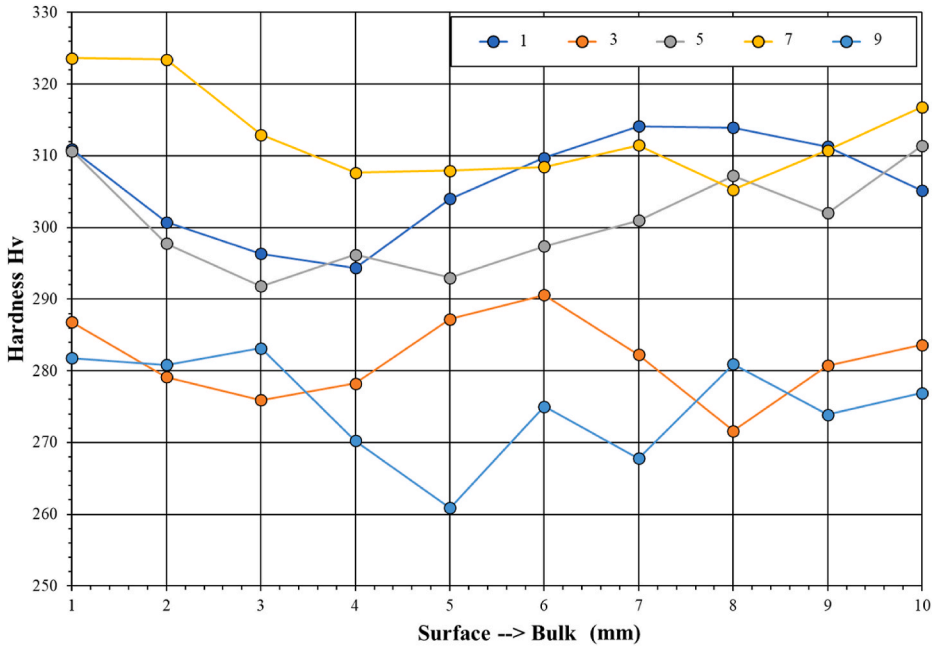

Fig. 20. Vicker's hardness results for as-built EBM Ti–6Al–4V samples. The first result for each specimen represents the indentation taken as close as possible to the surface location, but within the area requirements suitable for hardness testing.

Table 7
Vicker's hardness results for EBM Ti–6Al–4V machined & polished samples. The first result for each specimen represents the indentation taken as close as possible to the surface location, but within the area requirements suitable for hardness testing.

Sample	Hardness Hv										Stnd Dev
	1	2	3	4	5	6	7	8	9	10	
11	291	279	302	292	291	285	288	297	286	297	6.28
13	303	292	293	288	297	296	291	290	288	295	4.51
15	285	299	290	294	289	293	287	293	287	291	3.80
17	303	287	292	299	288	284	296	294	302	283	7.00
19	289	293	281	288	288	291	291	290	293	295	3.65

4. Conclusions

The main goal of this research was to understand the controlling influences on the fatigue behaviour of as-built and machined & polished EBM Ti–6Al–4V samples and to identify any correlation between the fatigue life, surface parameters and sample porosity. From this work, the following conclusions can be drawn:

- As-built samples have a significantly inferior fatigue life than that of machined & polished samples due to the high surface roughness, despite the material in each of the surface finish types being hot isostatically pressed.
- When compared to conventional material, the fatigue life of as-built EBM samples is significantly inferior, while machined & polished EBM samples have a fatigue life greater than conventionally cast and wrought material with the exception of conventional sheet material at stresses below 700 MPa.
- A decrease in a sample's R_p value results in an increase in the number of fatigue cycles a sample is able to withstand before failing increase. However, MR_2 and R_a values provide no correlation to the HCF life of EBM Ti–6Al–4V samples.
- The fracture surfaces of as-built samples tend to exhibit multiple zones of fatigue initiation from the sample surface, while machined & polished fracture surfaces have shown little evidence of fatigue initiating at surface regions with crack nucleation sites more associated with sub-surface features.
- Sample porosity influences the fatigue life of EBM Ti–6Al–4V no matter the surface condition and therefore, surface roughness cannot be considered the only detrimental factor to fatigue performance.
- The influence of surface finish has been shown to greatly influence the high cycle fatigue performance of EBM Ti–6Al–4V and a simplified, elastic finite element model has been used to predict the stress concentration factors at the idealised surface of an as built test specimen, where tentative values for K_t in excess of 3 are observed.
- The variation in material hardness from surface to interior bulk material is smaller in the machined & polished samples, than that seen in the as-built samples.
- In both the as-built and machined & polished samples, it can be determined that there are no extreme changes in material hardness from the surface to bulk material. With the minimal changes seen expected to be down to natural variation in sample material, this is not considered to have an impact in the fatigue life.

CRediT authorship contribution statement

L. Ednie: Writing – original draft, Writing – review & editing, Data curation, Investigation, Verification, Formal analysis, Visualization. **R. J. Lancaster:** Writing – original draft, Writing – review & editing, Conceptualization, Methodology, Supervision, Project administration, Funding acquisition. **A.A. Antonysamy:** Conceptualization, Methodology, Supervision, Project administration, Funding acquisition, Resources. **F. Zelenka:** Data curation, Visualization, Formal analysis. **A. Scarpellini:** Data curation, Visualization. **L. Parimi:** Methodology,

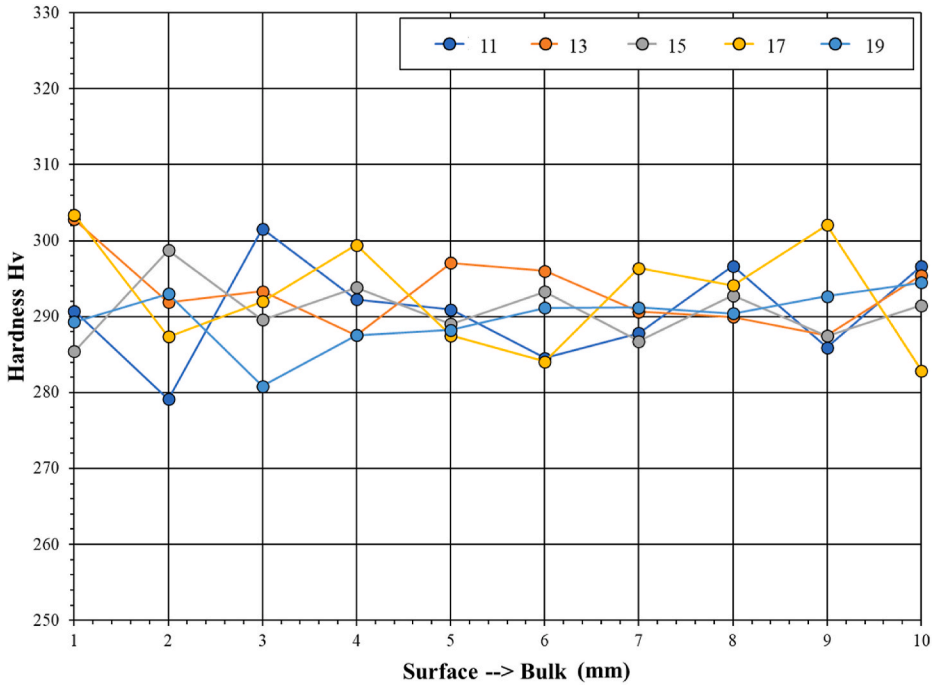

Fig. 21. Vicker's hardness results for machined & polished EBM Ti–6Al–4V samples. The first result for each specimen represents the indentation taken as close as possible to the surface location, but within the area requirements suitable for hardness testing.

Resources. **R. Maddalena:** Data curation, Visualization. **N.C. Barnard:** Visualization, Formal analysis. **P. Efthymiadis:** Supervision, Project administration.

Declaration of competing interest

The authors declare that they have no known competing financial interests or personal relationships that could have appeared to influence the work reported in this paper.

Data availability

The data that has been used is confidential.

Acknowledgements

The current research was funded by the Materials and Manufacturing Academy, M2A, (grant number: c80816) supported by the European Social fund through the Welsh Government. The provision of a research bursary, materials and supporting information from GKN Additive is gratefully acknowledged. The assistance provided by the Swansea University AIM Facility and the Welsh Coating and Printing Centre, which was funded in part by the EPSRC, are also much appreciated.

References

[1] T. Gornet, T. Wohler, History of Additive Manufacturing, vols. 1–34, 2014.
[2] S. Liu, Y.C. Shin, Additive manufacturing of Ti6Al4V alloy: a review, Mater. Des. 23 (2018).
[3] A. Uriondo, M. Esperon-Miguez, S. Perinpanayagam, The present and future of additive manufacturing in the aerospace sector: a review of important aspects, Proc. Inst. Mech. Eng. Part G J Aerosp Eng 229 (2015) 2132–2147.
[4] H.K. Rafi, N.V. Karthik, H. Gong, et al., Microstructures and mechanical properties of Ti6Al4V parts fabricated by selective laser melting and electron beam melting, J. Mater. Eng. Perform. 22 (2013) 3872–3883.
[5] P. Wang, W.J. Sin, M.L.S. Nai, et al., Effects of processing parameters on surface roughness of additive manufactured Ti-6Al-4V via electron beam melting, Materials 10 (2017) 11.
[6] J. Karlsson, Optimization of Electron Beam Melting for Production of Small Components in Biocompatible Titanium Grades, 2015.
[7] B. Bhushan, Surface roughness analysis and measurement techniques, in: Modern Tribology Handbook: Volume One: Principles of Tribology, CRC Press LLC, 2000, pp. 49–119.
[8] P. Dirisu, G. Supriyo, F. Martina, et al., Wire plus arc additive manufactured functional steel surfaces enhanced by rolling, Int. J. Fatig. 130 (2020), 105237.
[9] G. Nicoletto, R. Konečná, M. Frkáň, et al., Surface roughness and directional fatigue behavior of as-built EBM and DMLS Ti6Al4V, Int. J. Fatig. 116 (2018) 140–148.
[10] M. Kahlin, H. Ansell, D. Basu, et al., Improved fatigue strength of additively manufactured Ti6Al4V by surface post processing, Int. J. Fatig. 134 (2020), 105497.
[11] J. Gockel, L. Sheridan, B. Koerper, et al., The influence of additive manufacturing processing parameters on surface roughness and fatigue life, Int. J. Fatig. 124 (2019) 380–388.
[12] D. Greitemeier, C. Dalle Donne, F. Syassen, et al., Effect of surface roughness on fatigue performance of additive manufactured Ti–6Al–4V, Mater. Sci. Technol. 32 (2016) 629–634.
[13] S. Lee, Z. Ahmadi, J.W. Pegues, et al., Laser polishing for improving fatigue performance of additive manufactured Ti-6Al-4V parts, Opt Laser. Technol. 134 (2021), 106639.
[14] H. Javadi, W. Jomaa, D. Texier, et al., Surface roughness effects on the fatigue behavior of as-machined Inconel718, Solid State Phenom. 258 (2016) 306–309.
[15] N. Sanaei, A. Fatemi, Defects in additive manufactured metals and their effect on fatigue performance: a state-of-the-art review, Prog. Mater. Sci. 117 (2021), 100724.
[16] J.W. Pegues, N. Shamsaei, M.D. Roach, et al., Fatigue life estimation of additive manufactured parts in the as-built surface condition, Mater Des Process Commun 1 (2019) 3.
[17] C. Qiu, C. Panwisawas, M. Ward, et al., On the role of melt flow into the surface structure and porosity development during selective laser melting, Acta Mater. 96 (2015) 72–79.
[18] T. Debroy, H.L. Wei, J.S. Zuback, et al., Progress in materials science additive manufacturing of metallic components – process, Struct. Process 92 (2018) 112–224.
[19] British Standards Institution, European Committee for Standardization. BS EN 6072, BSI Standards Publication Aerospace Series — Metallic Materials — Test Methods — Constant Amplitude Fatigue Testing, 2010.
[20] Standardisation IO for. *ISO 21290-3:2021 Geometrical product specifications (GPS) - Surface Texture: Profile*. 2021.
[21] Standardisation IO for, ISO 1099:2006 Metallics Materials- Fatigue Testing - Axial Force-Controlled Method, 2006.
[22] ASTM International, Standard Test Methods for Vickers Hardness and Knoop Hardness of Metallic Materials, *ASTM E92-17* 2017; 1-27.
[23] M. Donachie Jr., Titanium: A Technical Guide, second ed., ASM International, 2000.
[24] ASTM International. Standard Test Methods for Determining Average Grain Size. *ASTM E112-10* 2010; 1–27.
[25] J. Lucas, P. Konieczny, Relationship between alpha grain size and crack initiation fatigue strength in Ti-6AI-4V, Metall. Mater. Trans. A Phys. Metall Mater. Sci. 2 (1971) 5–6.

[26] M. Kahlin, Fatigue Performance of Additive Manufactured Ti6Al4V in Aerospace Applications, Linkoping University, Sweden, 2017.
[27] R.C. Rice, J.L. Jackson, J. Bakuckas, et al., Federal Aviation Administration - Metallic Materials Properties Development and Standardization, DOT/FAA/AR-MMPDS-0, 2003.
[28] A.H. Chern, A review on the fatigue behavior of Ti-6Al-4V fabricated by electron beam melting additive manufacturing, Int. J. Fatig. 119 (2019) 173–184.
[29] J.H. Rao, N. Stanford, A survey of fatigue properties from wrought and additively manufactured Ti-6Al-4V, Mater. Lett. 283 (2021), 128800.
[30] T.L. Anderson, Fracture Mechanics: Fundaamentals and Applications, fourth ed., CRC Press LLC, 2017.
[31] C.C.C. Lesko, L.C. Sheridan, J.E. Gockel, Microhardness as a function of process parameters in additively manufactured alloy 718, J. Mater. Eng. Perform. 30 (2021) 6630–6639.
[32] F. Liu, C. He, Y. Chen, et al., Effects of defects on tensile and fatigue behaviors of selective laser melted titanium alloy in very high cycle regime, Int. J. Fatig. 140 (2020), 105795.
[33] E. Wycisk, A. Solbach, S. Siddique, et al., Effects of defects in laser additive manufactured Ti-6Al-4V on fatigue properties, Phys. Procedia 56 (2014) 371–378.